Interplay between Electronic, Magnetic, and Transport Properties in Metal Organic–Radical Frameworks

Nina Tymińska, Mikael Kepenekian

Interplay Between Electronic, Magnetic and Transport Properties in Metal Organic-Radical Frameworks

Nina Tymińska and Mikaël Kepenekian*

Univ Rennes, ENSCR, INSA Rennes, CNRS, ISCR (Institut des Sciences Chimiques de Rennes) - UMR 6226, F-35000 Rennes, France

Development of modern electronic and spintronic technologies depends in large part on the ability to design materials exhibiting switchable magnetic and electrical properties. Here, motivated by the successful demonstration of reversible redox switching of magnetic order and electrical conductivity in 2-dimensional metal-organic frameworks (MOFs) based on benzoquinoid linkers, we perform hybrid density functional theory calculations to investigate this phenomenon at the atomistic level. Electronic, magnetic and charge transport properties have been systematically investigated for oxidized and reduced forms of Mn and Fe benzoquinoid frameworks (i.e., $(Me_4N)_2[Mn_2L_3]$, $(Me_4N)_2[Fe_2L_3]$ and $Na_3(Me_4N)_2[Mn_2L_3]$, $Na(Me_4N)_2[Fe_2L_3]$, respectively with deprotonated chloranilic acid as L). We demonstrate that the experimentally observed large increase in electronic conductivity upon ligand-centered reduction in the Mn MOF (10^9 $S \cdot cm^{-1}$), is due to cooperative effects arising from band gap reduction and the presence of electrons with lower effective mass. Superior conductivity (by at least 3 orders of magnitude) of the redox pair of the Fe benzoquinoid framework as compared to the Mn analog stems from similar factors and, notably, a large increase in electron delocalization for the reduced Fe compound.

1 Introduction

Two-dimensional (2D) multifunctional materials with adaptable magnetic order and electrical conductivity have attracted significant interest in recent years as they open the door to realization of more complex and powerful electronic devices.[1–6] Traditionally, inorganic semiconductors have been used as functional electronic materials. However, despite their excellent properties, the limited capacity for pre- or post-synthetic manipulation as well as other key challenges,[7,8] such as controlled modulation of conductivity,[9,10] hinders the experimental realization of multi-switchable inorganic materials.[11–13] In contrast, metal-organic frameworks (MOFs), a class of hybrid organic-inorganic materials that crystallize by the assembly of metal ions and organic ligands to form 1-dimensional (1D), 2D or 3D extended structures with potential voids,[14,15] offer unprecedented structural and functional tunability for device implementation.[16–18] Historically, MOFs have been studied mostly because of their structural properties (porosity, breathing) for applications in gas storage/separation and catalysis[19] and to far less extent for their electronic, optical or magnetic properties.[13,20–23]

Stable organic radicals constitute a unique opportunity to design multifunctionality in extended systems.[5,24,25] Their open-shell spin doublet ground state (or higher for polyradicals) opens the door to magnetic properties and the manipulation of spins, *i.e.*, spintronics.[26,27] Importantly, organic radicals can be introduced into MOFs either

by pre-organization in a self-assembly process or post-synthetic modification of innocent ligand into its radical form.[28,29] Indeed, redox active ligands such as pyrizine,[30] 7,7,8,8-tetracyano-p-quinodimethane,[31] 2,5-dihydroxy-1,4-benzoquinone (anilic acid) and its derivatives[32–34] have been incorporated into some transition metal based MOFs that exhibit satisfactory conducting properties. These mixed valence systems are one of most promising multifunctional materials for advanced electronic devices employed in information storage/processing,[35] energy storage/conversion,[36,37] sensing[38,39] and switching technologies.[33,40]

Yet, despite this potential and considerable progress in fundamental understanding, design and discovery of multifunctional materials based on MOFs simultaneous incorporation of high conductivity (σ) and high magnetic phase transition temperature (T_c) remains challenging.[13,23,41,42] Indeed, ability to mutually switch σ and T_c in MOFs has been only recently achieved.[3,43] Mainly, redox pair of iron-benzoquinoid frameworks,[3] shown substantial increase in T_c (by about 100K) upon one-electron reduction of 2,5-dichloro-3,6-dihydroxy-1,4-benzoquinonate ligands (L^{2-}) accompanied by small decrease in the electrical conductivity from $\sigma = 1.4(7) \times 10^{-2}/1.0(3) \times 10^{-3}$ S·cm^{-1} (solvated/desolvated form) in $(Me_2NH_2)_2[Fe_2L_3]$, Me = methyl, to $\sigma = 5.1(3) \times 10^{-4}$ S·cm^{-1} in $(Cp_2Co)_{1.43}(Me_2NH_2)_{1.57}[Fe_2L_3]$. This result was then linked to improved metal-organic radical coupling (since all innocent L^{2-} were reduced to their radical forms, $L^{3-\bullet}$) that at the same time caused the loss of the mixed valency, which facilitate the charge transfer.[3] On the other hand, Liu *et al.*,[43] reported remarkable enhancement of σ (by 200 000-fold) and lower, yet considerable, increase in T_c value (by $\sim$ 40K) in analogous manganese compounds. This raise a question about origin of the change in electrical conductivity ($\Delta\sigma$), as in this case neither oxidized nor reduced form of Mn benzoquinoid framework comprise mixed-valent ligands ($L^{2-}/L^{3-\bullet}$). In fact, these authors rationalized lower conductivity of the reduced Mn compound compared to Fe analog by evoking the concept of better energetic alignment of redox potentials of Fe^{+3}/Fe^{+2} and $L^{2-}/L^{3-\bullet}$ pair than that of Mn^{+3}/Mn^{+2} and $L^{2-}/L^{3-\bullet}$.[43] This mismatch could also lead to considerably higher activation energy values for both reduced (by 0.25 eV) and oxidized (by 0.48-0.55 eV) Mn-benzoquinoid frameworks.[23] However, in literature, other concepts have been also evoked to explain origin of conductivity enhancement in MOFs. For example, Ziebel *et al.,*[44] have shown that more diffuse metal orbitals lead to better overlap with ligand orbitals, and thus more effective charge delocalization and higher electrical conductivity. Mainly, $\sigma_{[Cr_2(dhbq)_3]^{1.5-}} < \sigma_{[Ti_2L_3]^{2-}} \ll \sigma_{[V_2L_3]^{2-}}$, with mixed-valence Cr-, Ti- and V-based materials classified as weakly exchanging, strongly exchanging Robin-Day class II and class III,[45] respectively, where the much higher conductivity of $[Ti_2L_3]^{2-}$ is explained by an appropriate energy alignment of V-*3d* with respect to π* orbitals of the ligand.[44] While these examples demonstrate that mixed valency of ligands,[3] metals[46] or both[47] enables charge transfer, consistent with strong electronic coupling, the exact cause of such large $\Delta\sigma$ in Mn benzoquinoid framework has not been not determined before. This may be of interest to community as it is not the only MOF showing very large enhancement in electrical conductivity. For example, million-fold increase of σ in Fe_2(DSBDC) and Fe_2(DOBCD) compared to the Mn analogs was attributed to presence of weakly bound spin-down electrons of the Fe^{3+}.[48] Thus, by investigating the phenomenon at the atomistic level, one can provide key insights and engage the rational design of future multifunctional hybrid organic-inorganic materials..[49–51]

Here, we use first-principles calculations, based on hybrid density function theory (DFT), to shed new light on

the origin of $\Delta\sigma$ in multifunctional Mn and Fe MOFs based on benzoquinoid linkers. After a thorough description of the structural, electronic and magnetic properties of the materials, we use the Boltzmann approach to investigate their transport properties. Crucially, we find that redox doped electrons have lower density-of-states averaged effective mass and therefore higher mobility than the oxidized forms. This, along with the lowering of the band gap upon reduction, is the key reason for better conductivity. Moreover, Fe analogs exhibit superior conductivity as compared to Mn compounds for the same reasons boosted by improved electron delocalization, especially in the reduced form.

2 Computational Details

First-principles calculations are carried out at the DFT level using the Perdew-Burke-Ernzerhof hybrid functional (PBE0),[52] as implemented in CRYSTAL14.[53,54] Mn atoms are described with the Hay-Wadt small core effective pseudopotential along with the 411d311 basis set for valence electrons,[55,56] Fe atoms with the ECP10MFD potential[57,58] and basis set, contracted according to s411p411d411 scheme.[59] 3-1p1G,[60] 6-21G*,[61,62] 6-31d1,[60] 8-511G,[63] and 86-311G,[64] all-electron basis sets are used for H, C, N, O, Na, and Cl atoms, respectively.

Full geometry optimizations (*i.e.*, both ionic and cell shape relaxations) and subsequent vibrational frequency calculations are performed, starting from experimental data, with a 6×6×6 *k*-point mesh and a total energy convergency threshold of 10^{-10} Ha per unit cell. Electronic and magnetic properties are obtained from single-point calculations using 9×9×9 *k*-point mesh. Electronic transport properties are computed for the ground states of Mn and Fe compounds using an analytical solution of Boltzmann transport equations (BTE) taken at room temperature (295 K) as implemented in CRYSTAL17,[65,66] with even denser *k*-point mesh (12×12×12) in order to ensure convergence of transport coefficients. Further details on the computational approaches can be found in Supporting Information (SI).

3 Results and discussion

3.1 Structures and Models

Previously synthesized and experimentally characterized MOFs based on L^{2-} with and Mn and Fe as metal centers presents common features.[3,43] Both compounds crystallize in the $P\bar{3}1m$ space group. Their structure consists of 2D honeycomb-like $[M_2L_3]^{2-}$, M = Mn or Fe, anionic networks where metal nodes are connected to three organic ligands and finds itself in a quasi-octahedral O_h environment (Figure **1**A).

The layers of oxidized form of Mn-based compound, $(Me_4N)_2[Mn_2L_3]$, are stacked along the crystallographic c-axis in an eclipsed conformation, with Me_4N^+ cations intercalated between layers (left hand side of Figure **1**B).[43] While in case of its chemically reduced form, $Na_3(Me_4N)_2[Mn_2L_3]$, layers of metal-organic networks $[Mn_2L_3]^{5-}$ are separated by Me_4N^+ and Na^+ cations (right hand side of Figure **1**B). Let us note that the position of Na^+ cations could not be determined experimentally due to a lack of order. Therefore, Na atoms were randomly placed in the

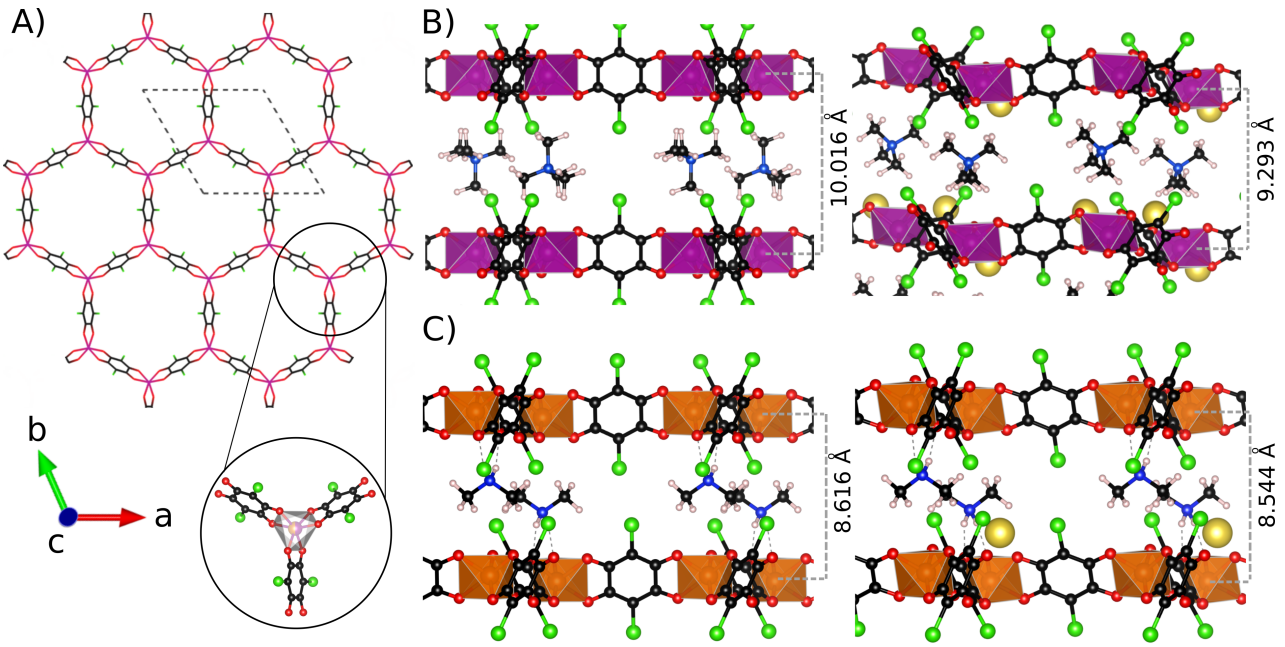

Figure 1 | A) Schematic depiction of the honeycomb-like lattice of the benzoquinoid-based MOFs with Mn and Fe. Organic cations have been omitted for clarity. The dashed rectangle marks the unit cell. B) and C) DFT optimized structures of ox-$[Mn_2L_3]^{2-}$ (left hand side), red-$[Mn_2L_3]^{5-}$ (right hand side) and ox-$[Fe_2L_3]^{2-}$ (left hand side), red-$[Fe_2L_3]^{3-}$ (right hand side), respectively. Mn, Fe, H, C, N, O, Na and Cl atoms are depicted in purple, orange, white, black, blue, red, yellow and green, respectively.

lattice prior to full geometry optimization.

Similar structures are found for the Fe compounds[3] (Figure **1** C). The oxidized form, $(Me_2NH_2)_2[Fe_2L_3]$, consists in layers of $[Fe_2L_3]^{2-}$, with Fe centers connected to mixed valent organic ligands (in 1:2 ratio of L^{2-} to $L^{3-\bullet}$), alternated with layers of $(Me_2NH_2)^+$ cations. Experimentally, the reduced form is determined to be $(Cp_2Co)_{1.43}(Me_2NH_2)_{1.57}[Fe_2L_3]$. In our model, in order to ease the comparison with the Mn compounds, the reduced form is taken as $Na(Me_2NH_2)_2[Fe_2L_3]$.

In both cases, DFT optimized structures are in good agreement with experimental data (Table S1 and S2).[3,43] From now on we will refer to oxidized and reduced forms of Mn and Fe benzoquinoid frameworks as ox-$[Mn_2L_3]^{2-}$, red-$[Mn_2L_3]^{5-}$ and ox-$[Fe_2L_3]^{2-}$, red-$[Fe_2L_3]^{3-}$, respectively.

3.2 Electronic structures

Figure **2** presents the band structures and projected density of states (pDOS) calculated for the Mn and Fe compounds. Ox-$[Mn_2L_3]^{2-}$, red-$[Mn_2L_3]^{5-}$ and ox-$[Fe_2L_3]^{2-}$ display indirect band gaps of 3.28 eV ($L \rightarrow \Gamma$), 2.18 eV ($\Gamma \rightarrow M$) and 1.62 eV ($K \rightarrow L$), respectively. On the other hand, red-$[Fe_2L_3]^{3-}$ is a direct semiconductor with band gap at A of 1.76 eV. Hence, upon reduction, the Mn compounds experience a significative lowering of its band gap (1.10 eV), while a small 0.14 eV increase is observed for Fe.

More importantly, all compounds exhibit low dispersive bands near the gap, a typical feature of semiconducting MOFs arising from weak hybridization of the orbitals of metal nodes and organic linkers.[48,67,68] This is particularly true for Mn compounds with bandwidths of top valence band and lower conduction band smaller than 30 meV (Figure S1) in both the oxidized and reduced form. The dispersions are also weak in the case of Fe compounds (less than 15 meV), with a sudden increase of the bandwidth of the top valence band of the reduced form to 195

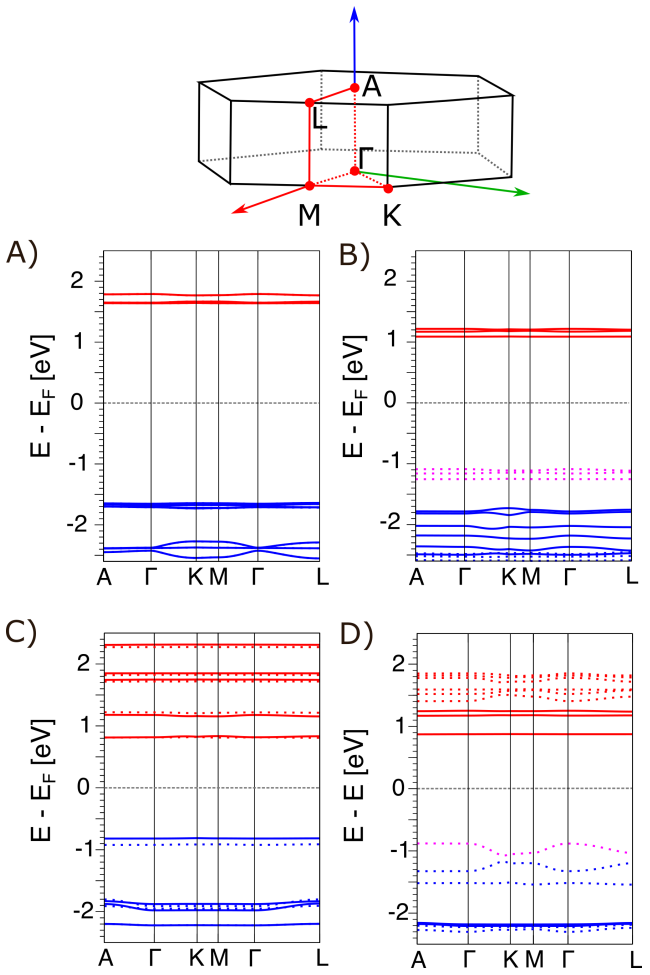

Figure 2 | DFT PBE0 calculated electronic band structures of ox-$[Mn_2L_3]^{2-}$ (panel A), red-$[Mn_2L_3]^{5-}$ (panel B), ox-$[Fe_2L_3]^{2-}$ (panel C) and red-$[Fe_2L_3]^{3-}$ (panel D). The Brillouin zone (shown in the inset) has been sampled at the special k-vector points of the $P\bar{3}1m$ space group. The valence and conductive bands are colored in blue and red, respectively with the solid-line indicating spin-up and dash-line indicating spin-down bands. Highlighted in pink are new valence bands appearing upon chemical reduction.

meV (Figure S2). Such features lead to large hole and electron effective masses (*vide infra*), detrimental to the mobilities of charge carriers.

Furthermore, projected density-of-states (pDOS) indicate that the valence band maximum (VBM) of ox-$[Mn_2L_3]^{2-}$ is predominantly composed of ligand-centered states with significant contribution from metal ions (formed by e_g^* type orbitals, *i.e.*, *d*–p_σ), while in red-$[Mn_2L_3]^{5-}$ contribution from Mn^{II} is essentially negligible (Figure **3**A and **3**B).

The conduction band minimum (CBM) in both forms of Mn benzoquinoid framework are mostly comprised of ligand states. This suggests that upon chemical reduction of ox-$[Mn_2L_3]^{2-}$ to red-$[Mn_2L_3]^{5-}$ manganese *3d* orbitals remain half-filled and previously unoccupied ligand-centered π^* orbitals are filled forming spin-down (noted as β-spin) band at higher energy. These low binding energy states give rise to new empty spin-up π^* (noted as α-spin) states that are located at lower energy levels than CBM of ox-$[Mn_2L_3]^{2-}$. In other words, simultaneous shift of both VBM and CBM arising from redox doping leads to a contraction of the band gap.

In case of ox-$[Fe_2L_3]^{2-}$ both VBM and CBM are mostly composed of ligand-centered states with non-negligible contribution from iron ions (Figure **3**C), hinting possibility of partial reduction of L^{2-} by Fe^{II}. Indeed, at +2 formal oxidation state iron is thought to spontaneously reduce L^{2-} to $L^{3-\bullet}$ during the synthesis.[1] This is also in line with

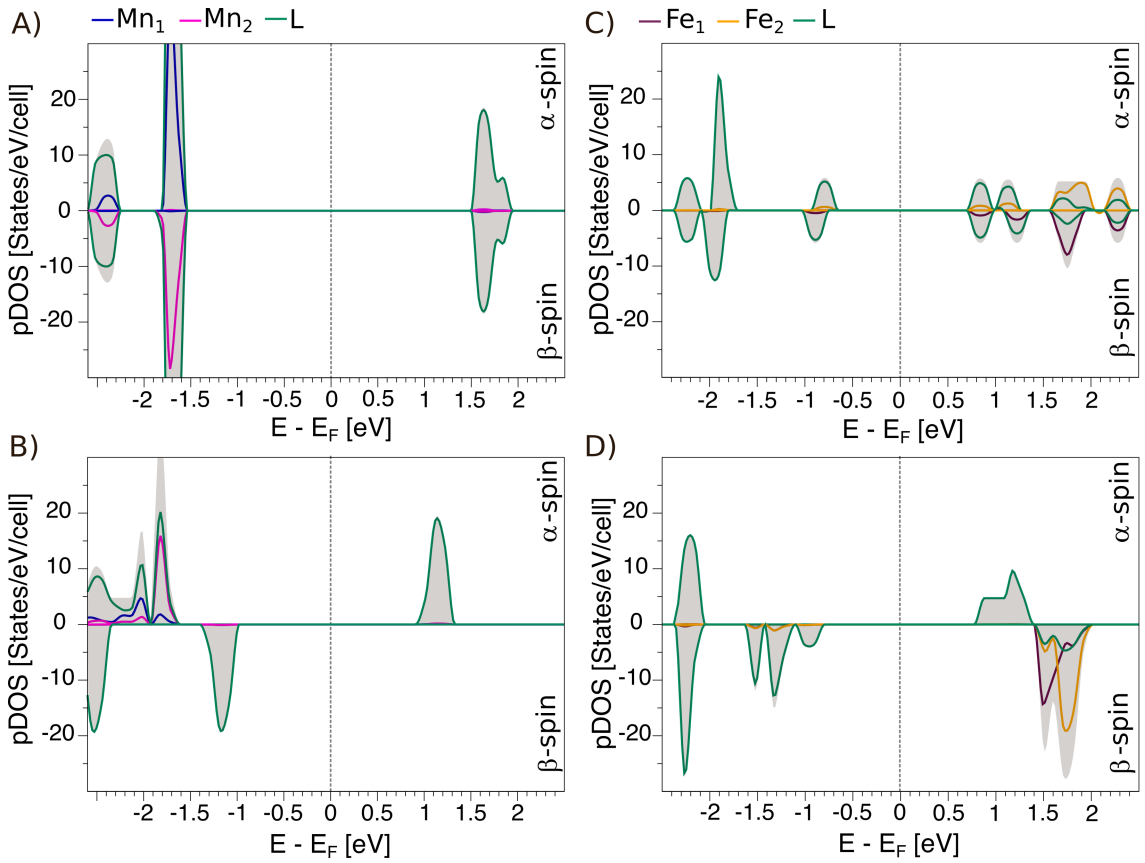

Figure 3 | DFT PBE0 calculated projected Densities of States (pDOS) of ox-$[Mn_2L_3]^{2-}$ (panel A), red-$[Mn_2L_3]^{5-}$ (panel B), ox-$[Fe_2L_3]^{2-}$ (panel C) and red-$[Fe_2L_3]^{3-}$ (panel D). Light gray area in pDOS plots represents total DOS.

analysis of pDOS of red-$[Fe_2L_3]^{3-}$, which shows that contribution from *Fe-3d* orbitals is only present in VBM (Figure **3**D). Once again *3d* orbitals of metal remain half-filled while the remaining L^{2-} are reduced. Mulliken spin population analysis further confirms that in both ox-$[Fe_2L_3]^{2-}$ and red-$[Fe_2L_3]^{3-}$ iron is at the same oxidation state (formally +3) and upon redox electron donation remaining L^{2-} are reduced (Table S3). Finally, as ox-$[Fe_2L_3]^{2-}$ consists of two-thirds of $L^{3-\bullet}$ previously noted small change in band gap caused by chemical reduction of the final (third) L^{2-} is expected. In both oxidized and reduced forms VBM is located nearly at the same energy located while CBM shifts to slightly higher energy level. Taken together foregoing results align with experimental chemical formula assignment,[3,43] *i.e.*, considered here systems in their reduced forms can be stated to be Mn^{II}/Fe^{III} and $3\times L^{3-\bullet}$, and in their oxidized forms Mn^{II} and $3\times L^{2-}$, Fe^{III} and $1\times L^{2-}$ and $2\times L^{3-\bullet}$.

In summary, analysis of electronic structure show that (i) chemical reduction of Mn benzoquinoid framework is accompanied by a dramatic decrease of the band gap and marginal increase in valence delocalization, (ii) by contrast redox electron donation to ox-$[Fe_2L_3]^{2-}$ leads to small increase in band gap and almost 1.5 order of magnitude increase in valence delocalization, (iii) in general Fe-based compounds exhibit smaller band gaps and more dispersed bands than both forms of Mn analogs, which imply better ligand-metal *p–d* orbital overlap (especially for lower energy t_{2g}^* type orbitals, *i.e.*, *d–π*) .

3.2.1 Effective masses and charge mobility

From foregoing analysis of band structures of Mn and Fe benzoquinoid frameworks one can expect high effective masses (m^*) for both positive (hole) and negative (electron) charge carriers, which can be indication of undesirable low charge carrier mobiliy (μ). This is because the latter is inversely proportional to the former via following relation $\mu = e\tau/m^*$.[69] Indeed, in general reported in Table 1 values of DOS-averaged effective masses of electron and hole ($m^*_{(e,h)_{DOS}}$) calculated from solution of BTE are very large and associated $\mu_{(e,h)}$ values are low for all considered compounds. Also, it is worth mentioning that calculated in-*ab*-plane $m^*_{(e,h)_{DOS}}$ values are typically 2 orders of magnitude smaller than those obtained for charge carriers moving out-of-plane (in *c*-axis direction). This gives higher $\mu_{(e,h)}$ values for both electrons and holes in the former than the latter direction. Anisotropic transport properties can be expected due to large separation between cations and anions of considered here compounds and absence of covalent boning in *c*-axis direction. Note that reported values are obtained at carrier density corresponding to chemical potential at VBM/CBM depending on a sign of charge carrier (Figures S3 and S4) at room temperature (295K). To the best of our knowledge charge mobilities of Mn and Fe benzoquinoid frameworks have not been determined before, therefore comparison with experiment is not possible at this point. Nevertheless, calculated $\mu_{(e,h)}$ values are comparable to those reported for some common hybrid organic-inorganic semiconductors.[23] For example, Mn_2(DSBDC)$(DMF)_2$ exhibits carrier mobility of 0.01 - 0.02 $cm^2{\cdot}V^{-1}{\cdot}s^{-1}$,[48,70] $K_xFe_2(BDP)_3$ from 0.02 to 0.84 $cm^2{\cdot}V^{-1}{\cdot}s^{-1}$,[71] and $Ni_3(HITP)_2$ 48.6 $cm^2{\cdot}V^{-1}{\cdot}s^{-1}$.[72]

Table 1 | Calculated charge carrier DOS-averaged effective masses ($m^*_{(e,h)_{DOS}}$) and mobilitities ($\mu_{(e,h)}$).

In-*ab*-plane	ox-$[Mn_2L_3]^{2-}$	red-$[Mn_2L_3]^{5-}$	ox-$[Fe_2L_3]^{2-}$	red-$[Fe_2L_3]^{3-}$
$m^*_{e_{DOS}}$ (m_0)	5.83×10^{2}	1.82×10^{2}	1.24×10^{3}	8.12×10^{-1}
$m^*_{h_{DOS}}$ (m_0)	4.15×10^{2}	4.65×10^{2}	3.97×10^{2}	8.17×10^{2}
μ_e ($cm^2{\cdot}V^{-1}{\cdot}s^{-1}$)	3.02×10^{-2}	9.64×10^{-2}	1.41×10^{-2}	2.17×10^{1}
μ_h ($cm^2{\cdot}V^{-1}{\cdot}s^{-1}$)	4.24×10^{-2}	3.79×10^{-2}	4.43×10^{-2}	2.15×10^{-2}
Out-of-plane				
$m^*_{e_{DOS}}$ (m_0)	4.08×10^{2}	1.72×10^{4}	9.51×10^{4}	4.56×10^{3}
$m^*_{h_{DOS}}$ (m_0)	1.23×10^{4}	5.37×10^{4}	1.32×10^{4}	1.62×10^{4}
μ_e ($cm^2{\cdot}V^{-1}{\cdot}s^{-1}$)	4.31×10^{-2}	1.02×10^{-3}	1.85×10^{-4}	3.86×10^{-3}
μ_h ($cm^2{\cdot}V^{-1}{\cdot}s^{-1}$)	1.43×10^{-3}	3.27×10^{-4}	1.33×10^{-3}	1.09×10^{-3}

out-off-plane = along the *c*-axis

$m_0 = 9.109 \times 10^{-31}$ kg (the free electron rest mass)

Importantly, this confirms that upon chemical reduction of L^{2-} to $L^{3-\bullet}$ in Mn benzoquinoid framework donated electrons are lighter (which feature may be associated with their weakly-bound character as discussed before) and therefore more mobile. Also, in case of red-$[Fe_2L_3]^{3-}$ $m^*_{e_{DOS}}/\mu_e$ is significantly lower/higher than for its oxidized form providing further evidence that valence band delocalization improves as more radical ligands is present in Fe benzoquinoid framework.

3.3 Magnetic properties

As shown in Figure **4**A the spin-unpaired electrons of ox-$[Mn_2L_3]^{2-}$ resides mostly on the metal nodes and as this compound undergoes single-crystal-to-single crystal one-electron reduction of each L^{2-} to $L^{3-\bullet}$ the spin density on oxygen and carbon atoms increases. This observation further confirms the formula proposed by Liu *et al.*,[43] ($[Mn_2L_3]^{5-}$) of red-$[Mn_2L_3]^{5-}$. In the case of ox-$[Fe_2L_3]^{2-}$ (Figure **4**B) both metal centers and two-thirds of the ligands possess unpaired electrons in perfect agreement with experimental results.[3] The third L^{2-} accepts redox donated electron to form fully reduced Fe benzoquinoid framework (red-$[Fe_2L_3]^{3-}$). Therefore in ox-$[Mn_2L_3]^{2-}$ the nearest neighbor spin partners are two Mn^{II}, while in the other compounds these are metal and radical ligand. Knowing this one can asses the coupling using mapping between model Hamiltonian and total DFT energy difference between states with a different electron configuration as briefly summarized below.

To investigate the magnetic properties of the Mn- and Fe benzoquinoid framework the ground-state electron charge density has been calculated, from which one can extract information on the total charge and spin distribution.[54,66] In addition, the strength of magnetic coupling (J) between spin-containing centers (MM - metal–metal, ML - metal–ligand) has been calculated by solving the Ising Hamiltonian,[73] defined in equation 1.

$$\hat{H} = -2\left(J_{MM}\sum_i \hat{S}_{M,i}\hat{S}_{M,i+1} + J_{ML^{3-\cdot}}\sum_i\left[(\hat{S}_{M,i}+\hat{S}_{M,i+1})\hat{S}_{L^{3-\cdot},i}\right]\right) \quad (1)$$

where $S_{M,i}$ and $S_{M,i+1}$ is a pair of arbitrary metal nodes, while $S_{L^{3-\cdot},i}$ is the i^{th} nearest neighbor radical ligand with spin S.

For an innocent ligand (S_L = 0) this expression becomes $E_{LS} - E_{HS} = 2JS_{M,1}S_{M,2}$, where E_{LS} and E_{HS} are total DFT energies of given system in overall low and high spin configuration. For HS magnetically isolated Mn^{II} and Fe^{III} S_M = 5/2. Note that the right hand side of equation 1 is often referred to as Seiden Hamiltonian model,[74] and can be used to obtain J-values for metal and radical ligand ($S_{L^{3-\cdot}}$ = 1/2), when $J_{MM} \approx 0$.

DFT calculations shows that energetically most stable state for oxidized form of Mn and Fe benzoquinoid frameworks correspond to total S = 0, which for the former represents a net repeating spin of unit containing two Mn^{II} centers that are antiferromagnetically (AFM) coupled and for the latter two Fe^{III} centers and two radical ligands that are AFM coupled (Figure **4**C).

However, due to large intralayer M$\cdots$M distances (about 8.0–8.1 Åfor M = Mn and 7.8–7.9 Åfor M = Fe) this interaction is very weak. Indeed, the calculated J_{MM} value for ox-$[Mn_2L_3]^{2-}$ is -0.7 meV (-5.6 cm^{-1}) and can therefore be neglected. On the other hand, the calculated couplings between metal and radical ligands $J_{ML^{3-\cdot}}$ are -13.1 meV (-105.7 cm^{-1}), -25.8 meV (-208.4 $cm^{-}1$) and -33.6 meV (-271.2 cm^{-1}), for red-$[Mn_2L_3]^{5-}$, ox-$[Fe_2L_3]^{2-}$ and red-$[Fe_2L_3]^{3-\bullet}$, respectively (relative energies used to calculate these values are provided in Table S4). Note that calculated $J_{ML^{3-\cdot}}$ of ox-$[Fe_2L_3]^{2-}$ is about two times higher than value obtained from experimental data fitting (-125.2 cm^{-1}), using an unspecified Hamiltonian.[75] It is well-known that hybrid functionals tend to overestimate J values,[76] this might also be the case here. More importantly, both ox-$[Fe_2L_3]^{2-}$ and red-$[Fe_2L_3]^{3-}$ exhibit stronger magnetic coupling than the Mn analogs, which is consistent with corresponding T_c values. Specifically, experimen-

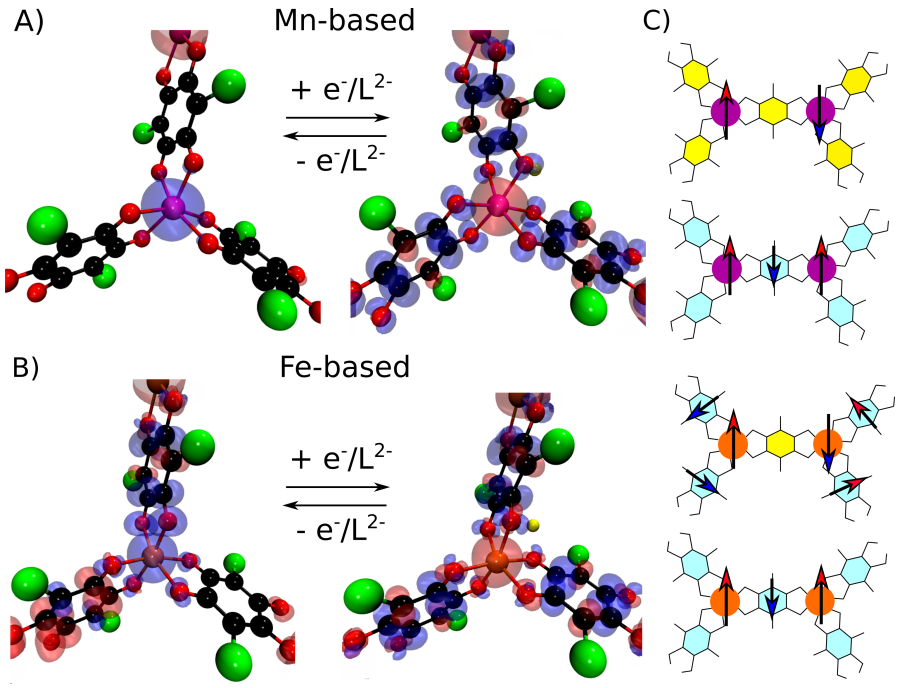

Figure 4 | A) and B) Spin density distribution ($\Delta\rho = \rho^{\alpha} - \rho^{\beta}$) in the selected fragment of corresponding Mn and Fe benzoquinoid frameworks. Red (blue) denotes the spin-up (spin-down) component. The isovalue for $\Delta\rho$ is $\pm$ 0.005 electron/bohr^{-3}. C) Schematic representation of spin alignment in units of ox-$[Mn_2L_3]^{2-}$, red-$[Mn_2L_3]^{5-}$ (top) and ox-$[Fe_2L_3]^{2-}$, red-$[Fe_2L_3]^{3-}$ (bottom). Yellow- and blue-filled hexagons represent oxidized (L^{2-}) and reduced ($L^{3-\bullet}$) benzoquinoid linkers, respectively and the purple and orange circles metal cations (Mn^{II} and Fe^{III}).

tally determined T_c for oxidized/reduced forms of Mn benzoquinoid framework is 1.8K/41K and for Fe analog it is 80K(26K^d)/105K (^{d}desolvated form of oxidized compound).[3,43] The contrast between Mn and Fe compounds can be understood when considering the simple case of two spin-1/2 magnetic centers antiferromagnetically coupled. The strength of the coupling then evolves like $-4t^2/U$ (the kinetic exchange), where t is the hopping integral between both centers and U the on-site repulsion.[77] The larger coupling observed in iron systems is the result of better hopping integrals between Fe and L than between Mn and L, as marked by wider peaks for Fe states in the density of states (Figure **3**) as well as the greater dispersion of valence states observed in Fe system band structures (Figure **2**).

3.4 Transport properties

In general many factors such as type of measurements (single crystal vs. polycrystalline pellets), disorder or defects, complicate to large degree the determination of the charge transport mechanism.[23] This in turn leads to the classification of conducting MOFs based on experimental approaches to design frameworks with high charge mobility and excellent electrical conductivity.[4,12,20,78,79] Charge transport in these materials can be described either by equations of the band transport regime (such as BTE) or those of hopping regime (typically based on Marcus theory).[80] The former is associated with dispersion of valence and conduction bands typically present in inorganic materials, while the latter with localized charges at discrete energy states (like in molecular conductors).[12,23] Often, conductivity in MOFs was determined to arise from charge hopping.[22,23,81] However, from a structural point of

view, aside of more complex crystal structure stemming from hybrid organic-inorganic nature of MOFs (featuring mixture of covalent and dispersive forces),[82] there is no difference between highly pure semiconducting MOFs and inorganic semiconductors. Furthermore, it is expected that both hopping and band-like transport mechanism yield low mobilities when band dispersion is weak.[83] In our case, the computed mobilities place us in an intermediate regime, at the limit of both charge hopping and band-like mechanisms.[80,84] We, therefore rely on BTE to describe the electronic transport properties of Mn and Fe systems. Yet, it remains a model and one should be mindful of its limitations.

Our calculations indicate that the largest change in electrical conductivity occurs when the chemical potential (ϕ) is equal to the Fermi level (E_F) located halfway between CBM and VBM, *i.e.*, in the middle of its band gap, which is characteristic of an undoped (intrinsic) semiconductors.[12,85] Hence we focus on the this region when discussing our results. However, because within the rigid-band approach, positive and negative ϕ values correspond to electron (n-type) and hole (p-type) type of doping, respectively,[86] we calculate the average electrical conductivity ($\sigma = \sum_{\alpha,\beta}(\sigma_{xx} + \sigma_{yy} + \sigma_{zz})/3$) as a function of ϕ in the range of $\pm$2.5 eV (Figure S5).

Figure **5**A shows the calculated σ at 295 K plotted as a function of the ϕ for both oxidized and reduced forms of Mn bezoquinoid framework. Specifically, for ox-$[Mn_2L_3]^{2-}$ $\sigma_{E_{F=0}}$ = 1.02×10^{-14} S·cm^{-1} and for red-$[Mn_2L_3]^{5-}$ $\sigma_{E_{F=0}}$ = 1.05×10^{-5} S·cm^{-1}, resulting in billion-fold increase in electrical conductivity. Liu *et al.,*[43] shown the 200 000-fold redox switching of electrical conductivity upon reduction of ox-$[Mn_2L_3]^{2-}$ to red-$[Mn_2L_3]^{5-}$, *i.e.*, σ value increasing from $1.14(3)\times10^{-13}$ S·cm^{-1} to $2.27(1)\times10^{-8}$ S·cm^{-1}. The difference between DFT and experimental $\Delta\sigma$ value is likely due in large part to expected difference between conductivity measurements for single-crystal vs. for polycrystalline. Specifically, pressed pallet (polycrystaline) measurements often only probe the inter-particle contacts, leading to much lower conductivities (by at least million times) than those determined based on the single-crystal measurements.[43,71] DFT model systems resemble the latter as calculations are performed on perfect single crystal. Our DFT calculations also recover the measured high anisotropy of red-$[Mn_2L_3]^{5-}$.[43] As can be seen in Figure **5**B in-*ab*-plane contributions to σ are significantly higher than those from out-of-plane. Indeed, calculated anisotropy σ_{ab}/σ_c values at $\phi = E_F$ are 2 and 75 for ox-$[Mn_2L_3]^{2-}$ and red-$[Mn_2L_3]^{5-}$, respectively. Noteworthy is that at chemical potential set at 0.6 eV below the VBM ($\phi - E_F \approx -1.7$ eV) anisotropy of red-$[Mn_2L_3]^{5-}$ reaches maximum value (within calculated ϕ range), *i.e.*, $\sigma_{ab}/\sigma_c \sim 600$. In case of ox-$[Mn_2L_3]^{2-}$ this occurs 0.7 eV above the middle of band gap, where $\sigma_{ab}/\sigma_c \sim 30$ (Figure S6).

In comparison Fe analog shows a modest change in conductivity (Figure **5**C), mainly calculated $\sigma_{E_{F=0}}$ = 3.92×10^{-3} S·cm^{-1} for ox-$[Fe_2L_3]^{2-}$ and for red-$[Fe_2L_3]^{3-}$ $\sigma_{E_{F=0}}$ = 2.58×10^{-2} S·cm^{-1}, which suggest that reduction of third L^{2-} to $L^{3-\bullet}$ may result in increase of σ by about one order of magnitude. At this point it should be noted that our calculated result is in stark contrast to experimental data provided in the work of DeGayner et al.[3] There are few possible reasons for this discrepancy: (i) model system is not representative of the compound, (ii) factors such as presence of defects or impurities not taken into account can greatly influence σ, and (iii) the calculated $\Delta\sigma$ is too small to determine if conductivity increased or decreased.

Figure **5**D shows that both oxidized and reduced forms of Fe bezoquinoid framework exhibit more anisotropic σ

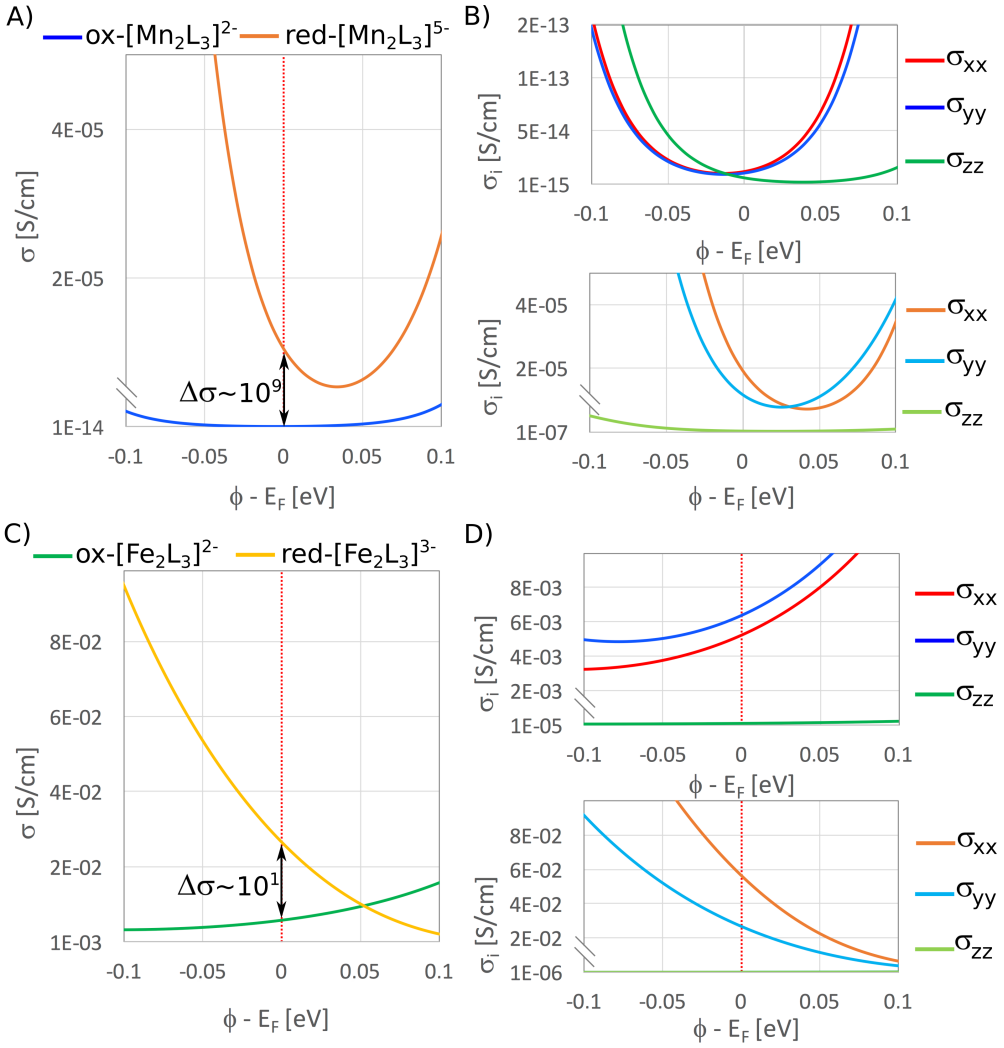

Figure 5 | A) and B) Average electrical conductivity, σ, as a function of the chemical potential, ϕ calculated for Mn and Fe bezoquinoid frameworks at room temperature (T = 295 K). C and D) corresponding in-*ab*-plane (σ_{xx}, σ_{yy} along a-, b-axis, respectively) and out-of-plane (σ_{zz} along c-axis) contributions to σ for oxidized (top) and reduced (bottom) forms of these materials. Fermi level is calculated via following expression $E_F = E_{VBM} - \frac{1}{2}\Delta E_g$ and $\sigma = \sum_{\alpha,\beta}(\sigma_{xx} + \sigma_{yy} + \sigma_{zz})/3$, $\sigma_i = \sum_{\alpha,\beta}\sigma_i$, where i = xx, yy or zz.

than corresponding Mn analogs, with σ_{ab}/σ_c values at $\phi = E_F$ are $\sim$ 30 and 2200 for ox-$[Fe_2L_3]^{2-}$ and red-$[Fe_2L_3]^{3-}$, respectively. Again, in-plane conductivity is dominating, especially in red-$[Fe_2L_3]^{3-}$, which is not surprising as dispersion of the valence band along Γ – K (or M–Γ) direction (k-points of Brillouin zone corresponding to sampling reciprocal-space in-plane of the crystal) is enhanced upon chemical reduction of ox-$[Fe_2L_3]^{2-}$ to red-$[Fe_2L_3]^{3-}$ (as mentioned before).

Furthermore our calculations confirm the predicted effect of metal exchange on MOF conductivity.[87] As shown in Figure **6**A, $\sigma_{\text{ox}-[Fe_2L_3]^{2-}} \gg \sigma_{\text{ox}-[Mn_2L_3]^{2-}}$ by about eleven orders of magnitude. Similarly, although to smaller extent $\sigma_{\text{red}-[Fe_2L_3]^{3-}} > \sigma_{\text{red}-[Mn_2L_3]^{5-}}$ for which $\Delta\sigma \sim 10^3$ (Figure **6**B). This results is also in an excellent agreement with experimental findings,[3,43] *i.e.*, comparing σ values for oxidized Mn and Fe benzoquinoid frameworks yields $\Delta\sigma \approx 1.0 \times 10^{11}$ S·cm^{-1} (or in case of desolvated form $\Delta\sigma \approx 9.0 \times 10^9$ S·cm^{-1}).

Overall, calculated electrical conductivity of Fe benzoquinoid framework is at least three orders of magnitude larger than that of Mn analog, which is due to both electronic and thermodynamic factors. We associate the former

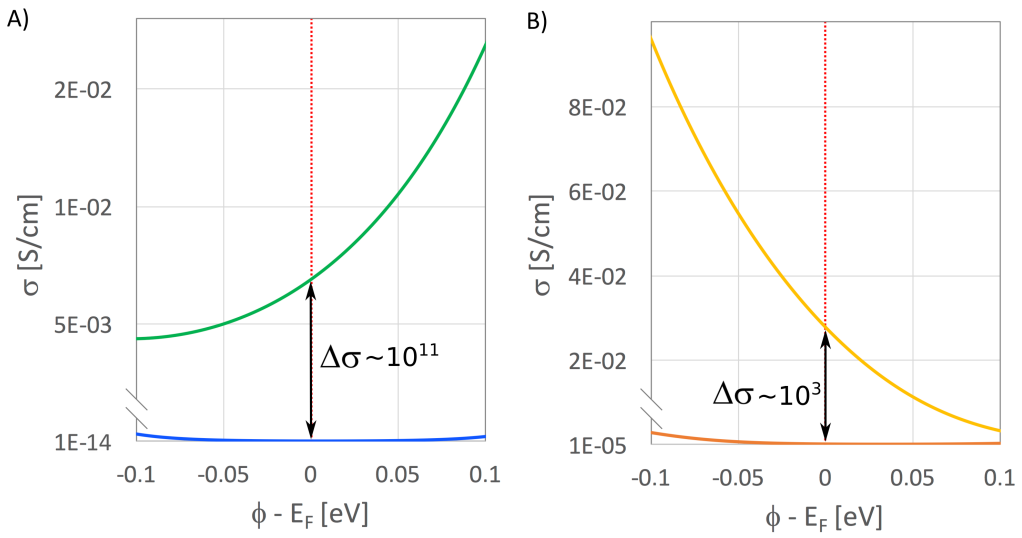

Figure 6 | Comparison of calculated electrical conductivities at T = 295 K of Fe and Mn benzoquinoid frameworks in their A) oxidized and B) reduced forms.

with better electron delocalization arising from larger valence band dispersion, especially in red-$[Fe_2L_3]^{3-}$, and the latter with smaller band gaps of oxidized and reduced forms of Fe than those in Mn compounds. It is known that activation energy, E_a, is related to the band gap, E_G, via the following expression, $E_G = 2\,E_a$.[12,78] Therefore minimizing E_G in MOFs is thought to improve conductivity. Impressive $\Delta\sigma$ linked to chemical reduction of organic ligand in Mn benzoquinoid framework originates from these factors as well, although in this case thermodynamic factor dominates. xCrucially, red-$[Mn_2L_3]^{5-}$ exhibits lighter electrons (i.e., with smaller $m^*_{e_{DOS}}$) that are easily accessible due to a VBM shift toward more positive (hence less bound) energy levels than those in ox-$[Mn_2L_3]^{2-}$. Finally, although technically calculated $\sigma_{\text{red}-[Fe_2L_3]^{3-}}$ is larger than $\sigma_{\text{ox}-[Fe_2L_3]^{2-}}$, despite of small increase in band gap (which can be easily overcome by improved valence electron delocalization), in comparison to other $\Delta\sigma$ values one can conclude that the conductivity values are comparable. Therefore full reduction of L^{2-} to $L^{3-\bullet}$ in Fe bezoquinoid framework can have a desired effect but we expect that even in the best case scenario it will be a very modest effect.

4 Concluding Remarks

In this work, using first principles calculations, we fully characterize electronic, magnetic and transport properties of Mn- and Fe benzoquinoid frameworks. Our DFT results confirm that the reduction turns innocent organic ligands (L^{2-}, S = 0) in non-innocent radicals ($L^{3-\bullet}$, S = 1/2). The latter have a sizeable antiferromagnetic coupling with the metal ions. Importantly, for both Mn and Fe, the presence of $L^{3-\bullet}$ in the network leads to greater delocalization of the charge due to better π-d overlap, an effect more pronounced in the Fe benzoquinoid framework than in the Mn analog. As a result, the experimentally observed impressive improvement of the conductivity ($\Delta\sigma$) upon reduction in the Mn benzoquinoid framework,[43] originates from cooperative thermodynamic (E_G lowering) and electronic (presence of light and therefore more mobile electrons) effects. On the other hand, the increase of conductivity in the Fe MOF, is the result of a competition between a small increase of the band gap compensated by a collapse of the effective masses. In general, DFT and Boltzmann theory calculations confirm importance of the electron

delocalization in increasing conductivity of MOFs, yet from aforementioned reasons it should not be treated as a golden rule. Finally we hope this work shows that accurate electronic structure modeling of MOFs is essential to fuel growing partnership between experiment and theory, which in turn is expected to accelerate development of multifunctional materials.

Acknowledgements

This work was supported by CNRS through the Emergence@INC 2020 call and granted access to the HPC resources of [TGCC/CINES/IDRIS] under the allocation 2019-A0090907682 made by GENCI. The authors thanks Boubacar Traoré for fruitful discussions.

Supporting information

The Supporting Information file contains: (i) Additional computational details including brief description of BTE as implemented in CRYSTAL17 (PDF), (ii) Further details on calculated properties of Mn- and Fe benzoquinoid frameworks (PDF), and (iii) PBE0 optimized structural models for oxidized and reduced Mn- and Fe benzoquinoid frameworks (CIF).

References

[1] Darago, L. E., Aubrey, M. L., Yu, C. J., Gonzalez, M. I. & Long, J. R. Electronic conductivity, ferrimagnetic ordering, and reductive insertion mediated by organic mixed-valence in a ferric semiquinoid metal-organic framework. *J. Am. Chem. Soc.* **137**, 15703–15711 (2015).

[2] Jeon, I.-R. *et al.* Solid-state redox switching of magnetic exchange and electronic conductivity in a benzoquinoid-bridged mn^{II} chain compound. *J. Am. Chem. Soc.* **138**, 6583–6590 (2016).

[3] DeGayner, J. A., Jeon, I.-R., Sun, L., Dincă, M. & Harris, T. D. 2d conductive iron-quinoid magnets ordering up to tc = 105 k via heterogenous redox chemistry. *J. Am. Chem. Soc.* **139**, 4175–4184 (2017).

[4] Stassen, I. *et al.* An updated roadmap for the integration of metal-organic frameworks with electronic devices and chemical sensors. *Chem. Soc. Rev.* **46**, 3185–3241 (2017).

[5] Ko, M., Mendecki, L. & Mirica, K. A. Conductive two-dimensional metal-organic frameworks as multifunctional materials. *Chem. Commun.* **54**, 7873–7891 (2018).

[6] Li, X., Li, X. & Yang, J. Two-dimensional multifunctional metal-organic frameworks with simultaneous ferro-/ferrimagnetism and vertical ferroelectricity. *J. Phys. Chem. Lett.* **11**, 4193–4197 (2020).

[7] MacDonald, A. H., Schiffer, P. & Samarth, N. Ferromagnetic semiconductors: Moving beyond (ga,mn)as. *Nat. Mater.* **4**, 195?202 (2005).

[8] Robinson, J. A. Perspective: 2d for beyond cmos. *APL Materials* **6**, 058202 (2018).

[9] He, T. *et al.* Controllable molecular modulation of conductivity in silicon-based devices. *J. Am. Chem. Soc.* **131**, 10023–10030 (2009).

[10] Deng, Y. *et al.* Gate-tunable room-temperature ferromagnetism in two-dimensional fe_3gete_2. *Nature* **563**, 94–99 (2018).

[11] Sheberla, D. *et al.* High electrical conductivity in ni_3(2,3,6,7,10,11-hexaiminotriphenylene)$_2$, a semiconducting metal-organic graphene analogue. *J. Am. Chem. Soc.* **136**, 8859–8862 (2014).

[12] Calvo, J. J., Angel, S. M. & So, M. C. Charge transport in metal-organic frameworks for electronics applications. *APL Materials* **8**, 050901 (2020).

[13] Rubio-Giménez, V., Tatay, S. & Martí-Gastaldo, C. Electrical conductivity and magnetic bistability in metal-organic frameworks and coordination polymers: Charge transport and spin crossover at the nanoscale. *Chem. Soc. Rev.* **49**, 5601–5638 (2020).

[14] Liu, W. *et al.* Structural engineering of low-dimensional metal-organic frameworks: Synthesis, properties, and applications. *Adv. Sci.* **6**, 1802373 (2019).

[15] Jiao, L., Seow, J. Y. R., Skinner, W. S., Wang, Z. U. & Jiang, H.-L. Metal-organic frameworks: Structures and functional applications. *Mater. Today* **27**, 43–68 (2019).

[16] Wang, C., Liu, D. & Lin, W. Metal-organic frameworks as a tunable platform for designing functional molecular materials. *J. Am. Chem. Soc.* **135**, 13222–13234 (2013).

[17] Zhai, Q.-G. *et al.* An ultra-tunable platform for molecular engineering of high-performance crystalline porous materials. *Nat. Commun.* **7**, 13645 (2016).

[18] Baumann, A. E., Burns, D. A., Liu, B. & Thoi, V. S. *Commun. Chem.* **2**, 86 (2019).

[19] Peplow, M. Materials science: The hole story. *Nature* **520**, 148–150 (2015).

[20] Stavila, V., Talin, A. A. & Allendorf, M. D. Mof-based electronic and opto-electronic devices. *Chem. Soc. Rev.* **43**, 5994–6010 (2014).

[21] Bhardwaj, S. K. *et al.* An overview of different strategies to introduce conductivity in metal-organic frameworks and miscellaneous applications thereof. *J. Mater. Chem. A* **6**, 14992–15009 (2018).

[22] Calbo, J., Golomb, M. J. & Walsh, A. Redox-active metal-organic frameworks for energy conversion and storage. *J. Mater. Chem. A* **7**, 16571–16597 (2019).

[23] Xie, L. S., Skorupskii, G. & Dincă, M. Electrically conductive metal-organic frameworks. *Chem. Rev.* **120**, 8536–8580 (2020).

[24] Maspoch, D., Ruiz-Molina, D. & Veciana, J. Old materials with new tricks: Multifunctional open-framework materials. *Chem. Soc. Rev.* **36**, 770–818 (2007).

[25] Clemente-León, M., Coronado, E., Martí-Gastaldo, C. & Romero, F. M. Multifunctionality in hybrid magnetic materials based on bimetallic oxalate complexes. *Chem. Soc. Rev.* **40**, 473–497 (2011).

[26] Hirohata, A. *et al.* Review on spintronics: Principles and device applications. *J. Magn. Magn. Mater.* **509**, 166711 (2020).

[27] Dieny, B. *et al.* Opportunities and challenges for spintronics in the microelectronics industry. *Nat. Electron.* **3**, 446–459 (2020).

[28] Faust, T. B. & D'Alessandro, D. M. Radicals in metal-organic frameworks. *RSC Adv.* **4**, 17498–17512 (2014).

[29] Souto, M., Strutyński, K., Melle-Franco, M. & Rocha, J. Electroactive organic building blocks for the chemical design of functional porous frameworks (mofs and cofs) in electronics. *Chem. Eur. J.* **26**, 1–25.

[30] Pedersen, K. S. *et al.* Formation of the layered conductive magnet $crcl_2(pyrazine)_2$ through redox-active coordination chemistry. *Nat. Chem.* **10**, 1056–1061 (2018).

[31] Miyasaka, H. *et al.* Control of charge transfer in a series of $ru_2^{II,II}$/tcnq two-dimensional networks by tuning the electron affinity of tcnq units: A route to synergistic magnetic/conducting materials. *J. Am. Chem. Soc.* **132**, 1532–1544 (2010).

[32] Mercuri, M. L., Congiu, F., Concas, G. & Sahadevan, S. A. Recent advances on anilato-based molecular materials with magnetic and/or conducting properties. *Magnetochemistry* **3**, 17 (2017).

[33] Murase, R., Leong, C. F. & D'Alessandro, D. M. Mixed valency as a strategy for achieving charge delocalization in semiconducting and conducting framework materials. *Inorg. Chem.* **56**, 14373–14382 (2017).

[34] Martínez-Hernández, C., Gómez-Claramunt, P., Benmansour, S. & Gómez-García, C. J. Pre- and post-synthetic modulation of the ordering temperatures in a family of anilato-based magnets. *Dalton Trans.* **48**, 13212–13223 (2019).

[35] Mezenov, Y. A., Krasilin, A. A., Dzyuba, V. P., Nominé, A. & Milichko, V. A. Metal-organic frameworks in modern physics: Highlights and perspectives. *Adv. Sci.* **6**, 1900506 (2019).

[36] Taniguchi, K., Chen, J., Sekine, Y. & Miyasaka, H. Magnetic phase switching in a tetraoxolene-bridged honeycomb ferrimagnet using a lithium ion battery system. *Chem. Mater.* **29**, 10053–10059 (2017).

[37] Ziebel, M. E. *et al.* Effects of covalency on anionic redox chemistry in semiquinoid-based metal-organic frameworks. *J. Am. Chem. Soc.* **142**, 2653–2664 (2020).

[38] Xiong, Y. *et al.* Synthesis of a mixed valence state ce-mof as an oxidase mimetic for the colorimetric detection of biothiols. *Chem. Commun.* **51**, 4635–4638 (2015).

[39] Zhang, J. *et al.* Mixed-valence cobalt(ii/iii) metal-organic framework for ammonia sensing with naked-eye color switching. *ACS Appl. Mater. Interfaces* **10**, 27465–27471 (2018).

[40] Ogihara, N., Ohba, N. & Kishida, Y. On/off switchable electronic conduction in intercalated metal-organic frameworks. *Sci. Adv.* **3** (2017).

[41] Li, W.-H., Deng, W.-H., Wang, G.-E. & Xu, G. Conductive mofs. *EnergyChem* **2**, 100029 (2020).

[42] Thorarinsdottir, A. E. & Harris, T. D. Metal-organic framework magnets. *Chem. Rev.* **120**, 8716–8789 (2020).

[43] Liu, L., DeGayner, J. A., Sun, L., Zee, D. Z. & Harris, T. D. Reversible redox switching of magnetic order and electrical conductivity in a 2d manganese benzoquinoid framework. *Chem. Sci.* **10**, 4652–4661 (2019).

[44] Ziebel, M. E., Darago, L. E. & Long, J. R. Control of electronic structure and conductivity in two-dimensional metal-semiquinoid frameworks of titanium, vanadium, and chromium. *J. Am. Chem. Soc.* **140**, 3040–3051 (2018).

[45] Robin, M. B. & Day, P. Mixed valence chemistry-a survey and classification. vol. 10 of *Advances in Inorganic Chemistry and Radiochemistry*, 247–422 (Academic Press, 1968).

[46] Xie, L. S. *et al.* Tunable mixed-valence doping toward record electrical conductivity in a three-dimensional metal-organic framework. *J. Am. Chem. Soc.* **140**, 7411–7414 (2018).

[47] Shilov, G. V., Nikitina, Z. K., Ovanesyan, N. S., Aldoshin, S. M. & Makhaev, V. D. Phenazineoxonium chloranilatomanganate and chloranilatoferrate: Synthesis, structure, magnetic properties, and mössbauer spectra. *Russ. Chem. Bull.* **60**, 1209–1219 (2011).

[48] Sun, L., Hendon, C. H., Minier, M. A., Walsh, A. & Dincă, M. Million-fold electrical conductivity enhancement in fe2(debdc) versus mn2(debdc) (e = s, o). *J. Am. Chem. Soc.* **137**, 6164–6167 (2015).

[49] Johnson, E. M., Ilic, S. & Morris, A. J. Design strategies for enhanced conductivity in metal-organic frameworks. *ACS Central Science* **0**, null (2021).

[50] Li, X. & Yang, J. Realizing two-dimensional magnetic semiconductors with enhanced curie temperature by antiaromatic ring based organometallic frameworks. *J. Am. Chem. Soc.* **141**, 109–112 (2019).

[51] Li, X. & Yang, J. Toward room-temperature magnetic semiconductors in two- dimensional ferrimagnetic organometallic lattices. *J. Phys. Chem. Lett.* **10**, 2439–2444 (2019).

[52] Adamo, C. & Barone, V. Toward reliable density functional methods without adjustable parameters: The pbe0 model. *J. Chem. Phys.* **110**, 6158–6170 (1999).

[53] Dovesi, R. *et al.* Crystal14: A program for the ab initio investigation of crystalline solids. *Int. J. Quantum Chem.* **114**, 1287–1317 (2014).

[54] Dovesi, R. *et al.* Crystal14 user's manual (2014). URL `https://www.crystal.unito.it/Manuals/crystal14.pdf`.

[55] Evarestov, R. A. *et al.* Comparative density-functional lcao and plane-wave calculations of $LaMno_3$ surfaces. *Phys. Rev. B* **72**, 214411 (2005).

[56] Evarestov, R., Kotomin, E., Heifets, E., Maier, J. & Borstel, G. Ab initio hartree-fock calculations of lamno3 (110) surfaces. *Solid State Commun.* **127**, 367–371 (2003).

[57] Dolg, M., Wedig, U., Stoll, H. & Preuss, H. Energy adjusted ab initio pseudopotentials for the first row transition elements. *J. Chem. Phys.* **86**, 866–872 (1987).

[58] Pseudopotential ecp10mdf for fe. URL `http://www.tc.uni-koeln.de/cgi-bin/pp.pl?language=en,format=crystal09,element=Fe`

[59] Basis set for fe. URL `http://www.crystal.unito.it/Basis_Sets/iron.html#Fe_ECP10MFD_s411p411d411_Heifets_2013`.

[60] Gatti, C., Saunders, V. R. & Roetti, C. Crystal field effects on the topological properties of the electron density in molecular crystals: The case of urea. *J. Chem. Phys.* **101**, 10686–10696 (1994).

[61] Catti, M., Pavese, A., Dovesi, R. & Saunders, V. R. Static lattice and electron properties of $MgCo_3$ (magnesite) calculated by ab initio periodic hartree-fock methods. *Phys. Rev. B* **47**, 9189–9198 (1993).

[62] Dovesi, R., Causa, M., Orlando, R., Roetti, C. & Saunders, V. R. Ab initio approach to molecular crystals: A periodic hartree-fock study of crystalline urea. *J. Chem. Phys.* **92**, 7402–7411 (1990).

[63] Dovesi, R., Roetti, C., Freyria-Fava, C., Prencipe, M. & Saunders, V. R. On the elastic properties of lithium, sodium and potassium oxide. an ab initio study. *Chem. Phys.* **156**, 11–19 (1991).

[64] Apra, E., Causa, M., Prencipe, M., Dovesi, R. & Saunders, V. R. On the structural properties of NaCl: An ab initio study of the b1-b2 phase transition. *J. Phys. Condens. Matter* **5**, 2969–2976 (1993).

[65] Dovesi, R. *et al.* Quantum-mechanical condensed matter simulations with crystal. *WIREs Comput. Mol. Sci.* **8**, e1360 (2018).

[66] Dovesi, R. *et al.* *CRYSTAL17 User's Manual* (Torino, Italy, 2017). URL `https://www.crystal.unito.it/Manuals/crystal17.pdf`.

[67] Pathak, A. *et al.* Integration of a (–cu–s–)n plane in a metal-organic framework affords high electrical conductivity. *Nat. Commun.* **10**, 1721 (2019).

[68] Gao, J. *et al.* A p-type ti(iv)-based metal-organic framework with visible-light photo-response. *Chem. Commun.* **50**, 3786–3788 (2014).

[69] Grosso, G. & Parravicini, G. P. *Solid State Physics* (Academic Press, 2014), 2 edn.

[70] Sun, L., Miyakai, T., Seki, S. & Dincă, M. Mn_2(2,5-disulfhydrylbenzene-1,4-dicarboxylate): A microporous metal-organic framework with infinite (-mn–s-)$_\infty$ chains and high intrinsic charge mobility. *J. Am. Chem. Soc.* **135**, 8185–8188 (2013).

[71] Aubrey, M. L. *et al.* Electron delocalization and charge mobility as a function of reduction in a metal-organic framework. *Nat. Mater.* **17**, 625–632 (2018).

[72] Wu, G., Huang, J., Zang, Y., He, J. & Xu, G. Porous field-effect transistors based on a semiconductive metal-organic framework. *J. Am. Chem. Soc.* **139**, 1360–1363 (2017).

[73] de Graaf, C. & Broer, R. *Magnetic Interactions in Molecules and Solids* (Springer International, 2016).

[74] Seiden, J. Propriétés statiques d'une chaîne isotrope alternée de spins quantiques 1/2 et de spins classiques. *J. Physique Lett.* **44**, 947–952.

[75] Chen, J. *et al.* Chameleonic layered metal-organic frameworks with variable charge-ordered states triggered by temperature and guest molecules. *Chem. Sci.* **11**, 3610–3618 (2020).

[76] Schweinfurth, D. *et al.* Tuning spin-spin coupling in quinonoid-bridged dicopper(ii) complexes through rational bridge variation. *Inorg. Chem.* **52**, 10332–10339 (2013).

[77] Malrieu, J. P., Caballol, R., Calzado, C. J., de Graaf, C. & Guihéry, N. Magnetic interactions in molecules and highly correlated materials: Physical content, analytical derivation, and rigorous extraction of magnetic hamiltonians. *Chem. Rev.* **114**, 429 (2014).

[78] Sun, L., Campbell, M. G. & Dincă, M. Electrically conductive porous metal-organic frameworks. *Angew. Chem. Int. Ed.* **55**, 3566–3579 (2016).

[79] Dong, R. *et al.* High-mobility band-like charge transport in a semiconducting two-dimensional metal-organic framework. *Nat. Mater.* **17**, 1027–1032 (2018).

[80] Oberhofer, H., Reuter, K. & Blumberger, J. Charge transport in molecular materials: An assessment of computational methods. *Chem. Rev.* **117**, 10319–10357 (2017).

[81] Leong, C. F., Usov, P. M. & D'Alessandro, D. M. Intrinsically conducting metal-organic frameworks. *MRS Bull.* **41**, 858–864 (2016).

[82] Rangel, T. *et al.* Structural and excited-state properties of oligoacene crystals from first principles. *Phys. Rev. B* **93**, 115206 (2016).

[83] Fumanal, M., Ortega-Guerrero, A., Jablonka, K. M., Smit, B. & Tavernelli, I. Charge separation and charge carrier mobility in photocatalytic metal-organic frameworks. *Adv. Funct. Mater.* **n/a**, 2003792.

[84] Troisi, A. The speed limit for sequential charge hopping in molecular materials. *Organic Electronics* **12**, 1988–1991 (2011).

[85] Xu, Y. & Schoonen, M. A. A. The absolute energy positions of conduction and valence bands of selected semiconducting minerals. *Am. Mineral.* **85** (2000).

[86] Ohkubo, I. & Mori, T. Two-dimensional layered complex nitrides as a new class of thermoelectric materials. *Chem. Mater.* **26**, 2532–2536 (2014).

[87] Sun, L. *et al.* Is iron unique in promoting electrical conductivity in mofs? *Chem. Sci.* **8**, 4450–4457 (2017).